Chapter 6
Design for Crashworthiness

One of the primary functions of the automobile body is to protect occupants in a collision. Because of the variability of field impacts, many governments have defined standard crash tests and minimum performance levels. For the USA, these standards are contained in the Federal Motor Vehicle Safety Standards [1], with similar standards for the European Union, Japan, Korea, Australia, and others.

6.1 Standardized Safety Test Conditions and Requirements

For impact tests which influence the overall vehicle structure, these standard tests may be categorized into four major groups: front impact, side impact, rear impact, and roll-over resistance. Figure 6.1 and Figure 6.2 illustrate the test conditions for these four groups.

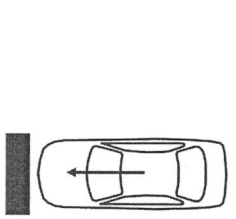

30mph Impact into rigid barrier

Criterion: Occupant injury

Front barrier

FMVSS 208

(a)

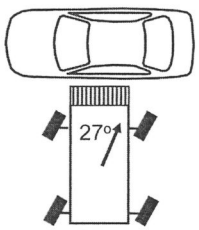

33.5 mph Impact by deformable moving barrier

Criterion: Occupant injury

Side barrier

FMVSS 214

(b)

Figure 6.1 Primary mandated crashworthiness requirements: Front and side impact.

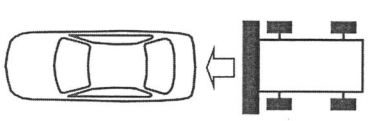

30mph Impact by moving barrier
Criterion: Fuel system integrity

Rear barrier

FMVSS 301

(a)

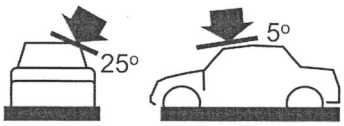

Load 1½ times vehicle weight
Criterion: Less than 5 inches of deformation

Roof crush

FMVSS 216

(b)

Figure 6.2 Primary mandated crashworthiness requirements: Rear and roof impacts.

These government standards establish a *minimum* performance level for the vehicles to be sold in the respective country. The insurance industry and consumer groups have developed tests which evaluate vehicles *beyond* the minimum government standards. The New Car Assessment Program (NCAP) is one such set of tests. The NCAP evaluation is based on the probability of injury for a specific test, measured with a star scale ranging from one star—higher probability of injury, to five stars—lower probability of injury, Figure 6.3.

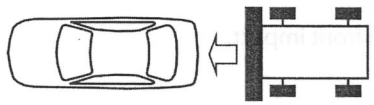

US-NCAP Front barrier:
35mph full face rigid barrier

Criterion: Star rating based on combination of head injury criteria (HIC) and chest acceleration for driver and passenger

% chance of serious injury		
	Frontal 35mph	Side 33mph
★★★★★	<10%	<5%
★★★★	11-20	6-10
★★★	21-35	11-20
★★	36-45	21-25
★	>46	>26

Star rating system

Figure 6.3 Customer-based crashworthiness: New car assessment program.

While these standards are extensive and cover many test configurations, we shall focus on two important conditions: full front barrier and side impact. By examining these two conditions in detail, we will develop general approaches and tools which can be used to examine other conditions.

6.2 Front Barrier

In this section, we will look at the condition of a moving vehicle impacting a rigid barrier. Although this is but one of several conditions for front impacts, the physical understanding and analysis we develop for this test case may be expanded for other conditions. The test conditions are shown in Figure 6.4. A vehicle of mass M is moving at a constant speed, V. It will just touch the rigid, unmovable barrier at time $t=0$. As the vehicle deforms, the speed of the vehicle center-of-mass will gradually reduce until it reaches $V=0$ at which time a maximum deformation, Δ, occurs. Figure 6.4b illustrates the vehicle before and after the test.

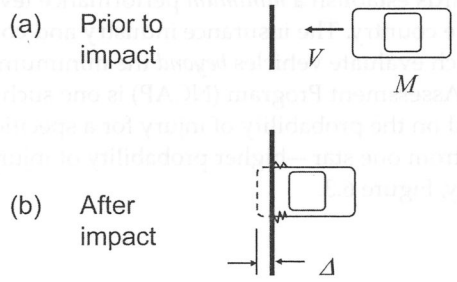

Figure 6.4 Full front impact.

Let us look at the sequence of events for a typical midsized vehicle as it undergoes such an impact, Figure 6.5 [2]. At time *t=0* the vehicle is moving at velocity $V=V_O$ and the front bumper is just touching the barrier face. At time *t=15 msec*, the bumper has collapsed and the motor compartment midrails and side rails are being loaded. At *t=30 msec* the mid rails have begun to crumple in an accordion fashion, and the powertrain has just touched the barrier and begins to decelerate. At *t=45 msec*, the midrails and upper rails continue to crumple, the powertrain has decelerated to zero velocity and the wheels have impacted the barrier. Finally at *t=90 msec*, the vehicle has decelerated to *V=0* with the motor compartment crumpled by some deformation, *Δ*.

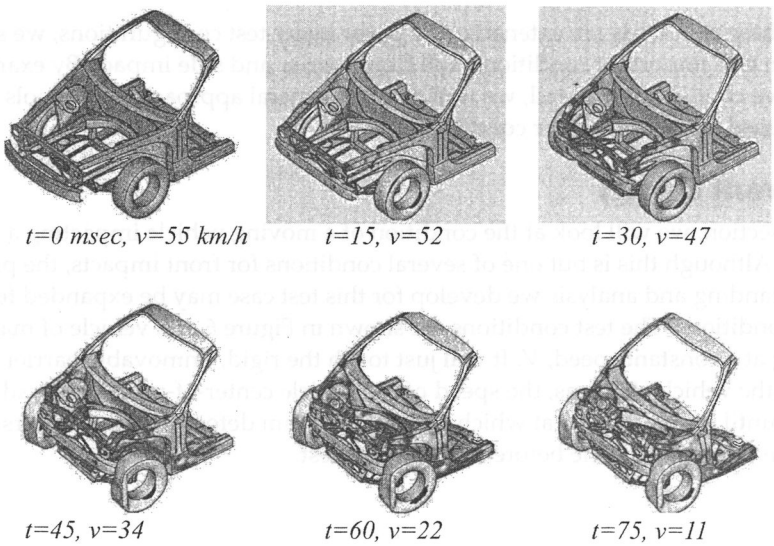

Figure 6.5 Typical front barrier sequence of events. (Courtesy of the American Iron and Steel Institute, UltraLight Steel Auto Body)

For this test, primary data are collected on the load applied to the barrier face and on the acceleration of the vehicle mass center. The acceleration is then integrated to determine velocity. Figure 6.6a [2] shows a typical graph for barrier face load vs. time. Early in the crash event, we see relatively low loads generated by the bumper collapsing, followed by a spike when the midrails are initially loaded. Another spike occurs at *t=35 msec* when the rigid powertrain impacts the barrier and is suddenly decelerated. This is followed by a relatively constant load for the rest of the event as the motor compartment structure continues to crumple.

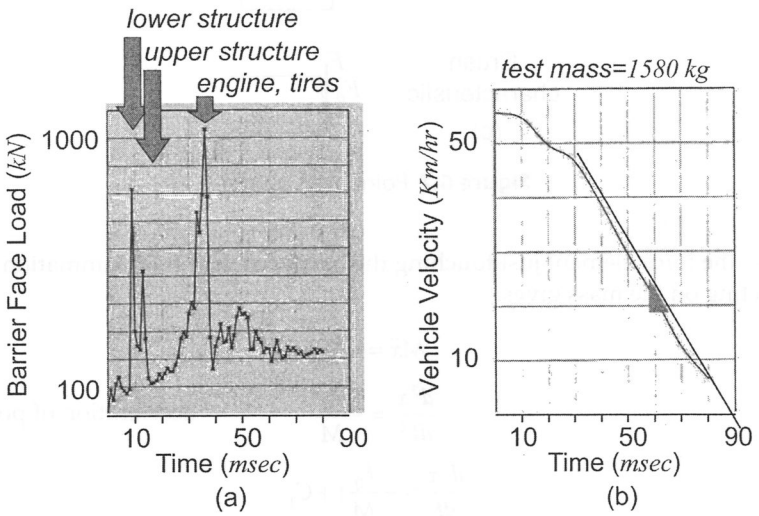

Figure 6.6 Typical front barrier time histories. (Courtesy of the American Iron and Steel Institute, UltraLight Steel Auto Body)

The corresponding graph of vehicle mass center velocity vs. time is shown in Figure 6.6b. Note that the slope of this curve at any time, *t*, is the acceleration of the vehicle mass center at that time. Velocity initially reduces gradually up to *t=30 msec* followed by a steeper linear reduction through the end of the event. The slope during this linear velocity reduction is the cabin deceleration.

For such a test we are interested in minimizing occupant injury. A first-order indication of this injury is given by the acceleration of the vehicle center of mass—a lower level of acceleration is less injurious. Let us consider the most basic analytical model to describe the impact and the resulting acceleration.

6.2.1 Basic kinematic model of front impact

Let us model this event with a point mass, *M*, representing the mass of the vehicle [3]. Attached to this mass is an element which generates a constant force, F_0, as it collapses, representing the crumpling front structure, Figure 6.7. We wish to develop graphs similar to Figure 6.6b for acceleration, velocity, and deformation for this simple model.

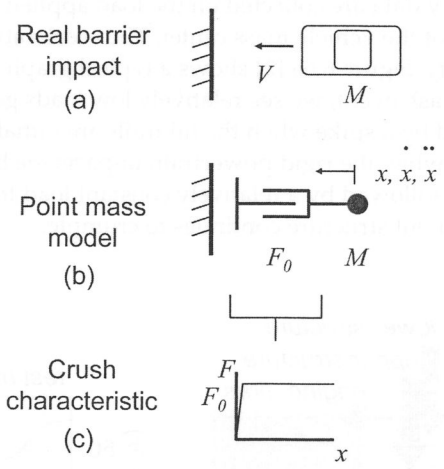

Figure 6.7 Point mass model.

Consider the force element just touching the barrier at time $t=0$. Summation of forces acting on the mass gives:

$$M\ddot{x} = -F_0$$

$$\frac{d^2x}{dt^2} = -\frac{F_0}{M} \qquad \text{acceleration of point mass}$$

$$\frac{d\,x}{dt} = -\frac{F_0}{M}t + C_1$$

The initial conditions are at $t=0$, $dx/dt=Vo$, the impact speed. Therefore,

$$\frac{d\,x}{dt} = -\frac{F_0}{M}t + V_0 \qquad \text{velocity of point mass}$$

Integrating a second time:

$$x = -\frac{F_0}{2M}t^2 + V_0 t + C_2$$

The initial conditions are at $t=0$, the deformation of the vehicle front end is zero or $x=0$:

$$x = -\frac{F_0}{2M}t^2 + V_0 t \qquad \text{deformation for point mass}$$

Finally, we can ask at what time, t_{FINAL}, is the crash event completed. This occurs when $dx/dt=0$, or:

$$\frac{d\,x}{dt} = -\frac{F_0}{M}t_{FINAL} + V_0 = 0$$

final time for point mass: $t_{FINAL} = \dfrac{MV_0}{F_0}$

The resulting behavior for this point mass model is shown in Figure 6.8.

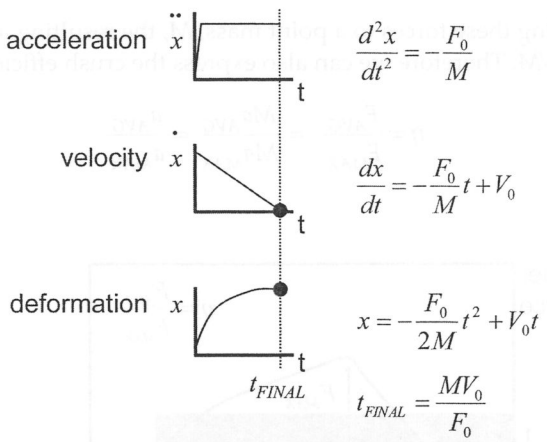

Figure 6.8 Behavior of point mass model.

Example: Point mass impact behavior

Consider a vehicle of mass *1580 kg*, impacting a rigid barrier at *55 kph*, and an average motor compartment crush load of *300 KN*. Applying the above equations, the acceleration is:

$$\frac{d^2x}{dt^2} = -\frac{F_0}{M} = \frac{300{,}000N}{1580kg} = 189.87m/\sec^2 = 19.37g$$

The time at the end of the crash event is:

$$t_{FINAL} = \frac{MV_0}{F_0} = \frac{1580kg(55kph)(1000m/km)/(3600\sec/hr)}{300000N} = 0.0805\sec$$

The total deformation at t_{FINAL} is:

$$x = -\frac{F_0}{2M}t^2 + V_0 t =$$
$$= -\frac{300000N}{2(1580kg)}(.0805\sec)^2 + (55kph)(1000m/km)/(3600\sec/hr)(.0805\sec) =$$
$$x = 0.614m$$

We can see by comparison of the velocity history with Figure 6.6b that this very simple model can reasonably predict impact behavior.

In this initial model we have assumed an ideal case of uniform load, F_0, as the structure collapses, Figure 6.7c. Let us refine the model by allowing crush force properties other than uniform. In Figure 6.9 we show a load-deformation curve with the same area under the curve as the square wave used before. (Thus each curve will result in the same work during deformation.) We can characterize this curve by a crush efficiency factor,

$$\eta = \frac{F_{AVG}}{F_{MAX}} \quad (0 < \eta < 1) \tag{6.1}$$

As we are applying these forces to a point mass, M, the resulting acceleration for the mass will be $a=F/M$. Therefore we can also express the crush efficiency factor as

$$\eta = \frac{F_{AVG}}{F_{MAX}} = \frac{Ma_{AVG}}{Ma_{MAX}} = \frac{a_{AVG}}{a_{MAX}} \tag{6.2}$$

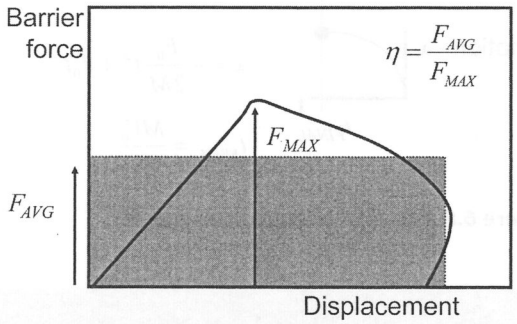

Figure 6.9 Characterizing barrier force.

We can now ask which of the four deformation curves of Figure 6.10a is preferable in minimizing occupant injury. Each of these deformation curves was applied to an occupant injury model with the resulting head acceleration shown in Figure 6.10b. The more square-shaped the curve, η approaching one, the lower the head injury. Thus, as we design the collapsing structure of the motor compartment, we will attempt to approach a square wave shape.

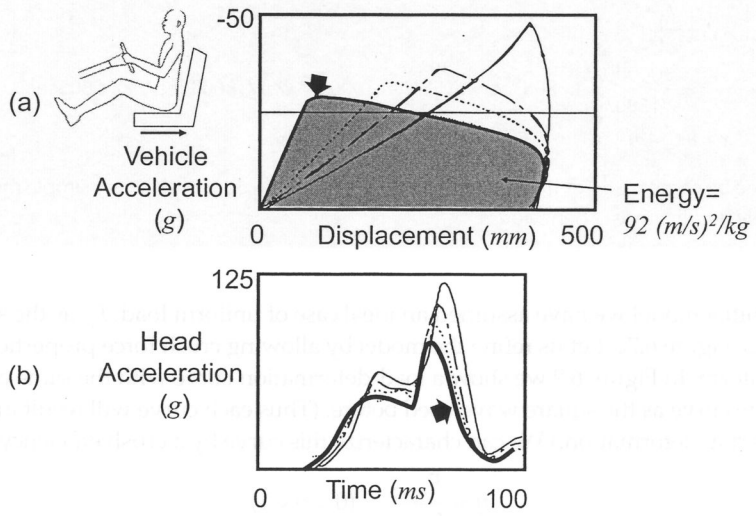

Figure 6.10 Effect on injury of acceleration pulse shape.

Now that we have established the general shape for the cabin acceleration, let us consider the magnitude of the peak acceleration. Figure 6.11 illustrates the velocity-time histories for several vehicles in a *30 mph (48 km/h)* front barrier test. Looking at the slope of these curves, we see a range of *20 g* to *30 g* for peak acceleration. In general, a lower peak cabin acceleration is less injurious, and we take the lower end of this benchmark data, *20 g*, as a target.

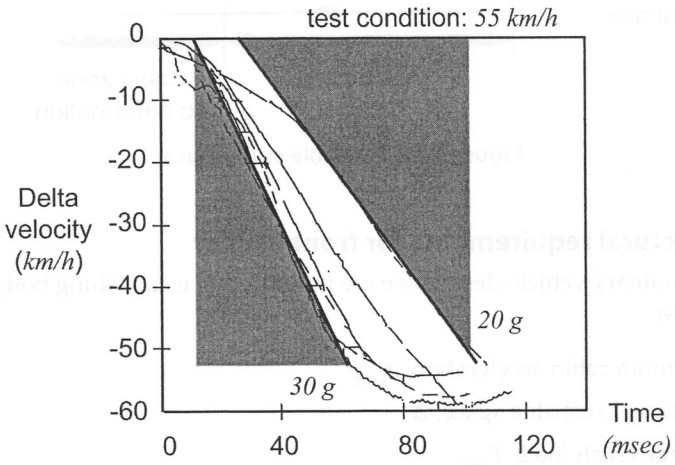

Figure 6.11 Typical velocity-time histories.

To summarize, we have established desirable characteristics for cabin acceleration during impact. First, limit maximum acceleration to approximately *20 g*, and second, make this acceleration as uniform as possible, that is make $\eta=a_{AVG}/a_{MAX} \sim 1$. These characteristics for cabin acceleration are directly related to front structure requirements since the inertia loads are those to be reacted by the structure.

The crushable space in the motor compartment, Figure 6.12, is an important variable in body design, as we will show in the next section. To measure this space, we first identify the cabin zone which we desire to keep from deforming. Ideally this zone wraps completely around the passengers. In practice, we can accept some amount of intrusion into the toe pan area on the order of *50 mm* to *120 mm (2 in. to 4.75 in.)* without increasing injury. The crush zone extends forward from the cabin zone to the front of the vehicle. The crush space, Δ, is the fore-aft dimension of the crush zone less the stack-up of rigid elements within that zone. Some subsystems within the crush zone are completely rigid, such as the engine block, and their total fore-aft dimension must be subtracted. Others can be crushed to some degree, and we make some assumption as to their final crush dimensions for inclusion in the crush space. For example, the radiator is assumed to crush to *50%* of its original thickness.

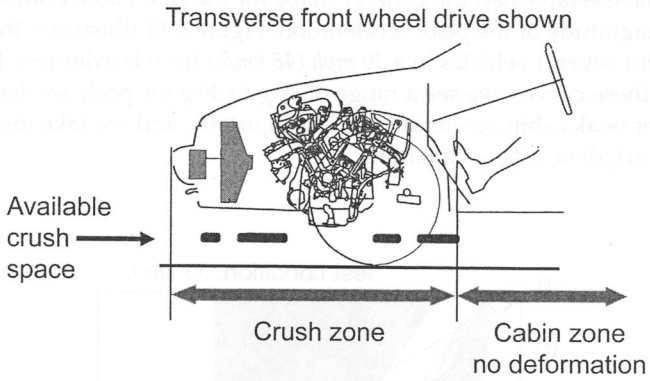

Figure 6.12 Available crush space.

6.2.2 Structural requirements for front barrier

During preliminary vehicle design, we are interested in establishing body structural requirements:

1. The maximum cabin acceleration, a_{MAX}
2. The necessary crushable space, Δ
3. The average crush force, F_{AVG}

These requirements cannot be set independently. We will show this by looking at a work-energy balance of the vehicle before and after impact.

Consider the vehicle immediately before impact, Figure 6.13a. The kinetic energy is $\frac{1}{2}MV_0^2$ where V_0 is the impact speed for the test. After impact we have zero kinetic energy, but work has been done to the system during collapse equal to the average crush force over the crush distance, $F_{AVG}\Delta$, Figure 6.13b. Equating kinetic energy to work done

$$\frac{1}{2}MV_0^2 = F_{AVG}\Delta$$

and substituting $F_{AVG}=\eta F_{MAX}$ and $F_{MAX}=a_{MAX}$ yields

$$a_{MAX} = \frac{V_0^2}{2\eta\Delta} \tag{6.3}$$

which is a relationship between maximum cabin acceleration, a_{MAX}, (which is related to occupant injury), crush space, Δ, (which is related to vehicle styling and packaging), crush efficiency, η, (which is related to body structure performance), and test speed, V_0. If we look at benchmark test data, Figure 6.14, we can see the inverse relationship between maximum cabin acceleration during impact and crush space. This illustration also shows the practical maximum value for crush efficiency, $\eta \sim 0.8$, when using crumpling of thin-walled structures as the energy-absorbing mechanism.

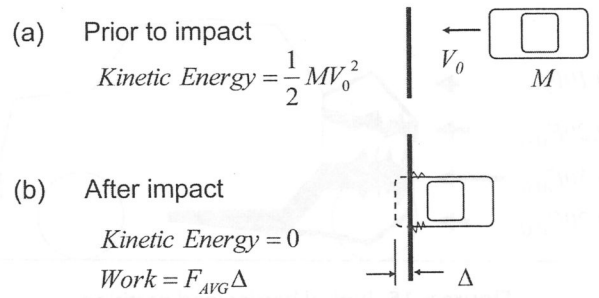

Figure 6.13 Full front impact.

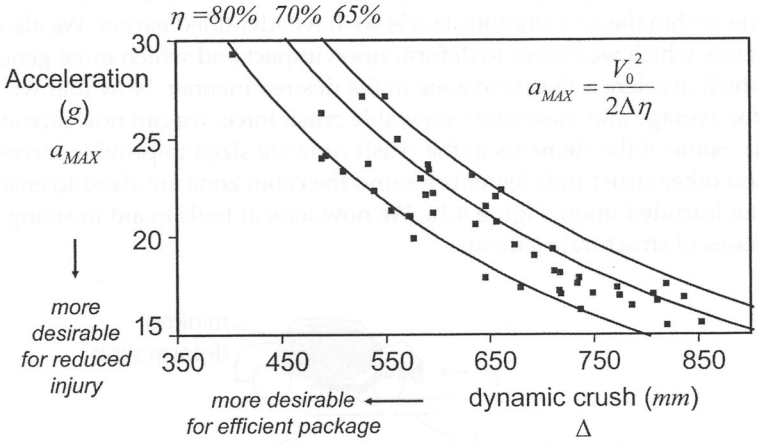

Figure 6.14 30 mph barrier benchmarking.

The relationship of Equation 6.3 suggests a procedure for establishing front body structural requirements for crashworthiness:

1. Determine the maximum allowable cabin decelerations based on occupant injury, a_{MAX}
2. Determine a consistent structural efficiency and crush space, ($\eta\Delta$?? using Equation 6.3
3. Compute the average and maximum allowable crush forces which the vehicle must generate during impact, F_{AVG}, F_{MAX}, using the efficiency, η, from step 2
4. Allocate these total forces from step 3 to the structural elements within the vehicle front end.

Some rules of thumb exist for this allocation of step 4: *20%* of the force is generated by the upper structure load path just under the top of fender, *50%* of the force is generated by the mid-rail structure, *20%* by the lower cradle, and *10%* by the hood and fenders, Figure 6.15.

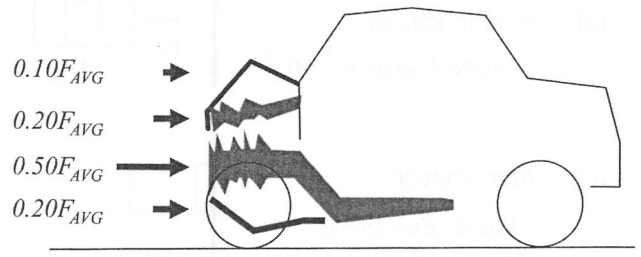

Figure 6.15 Typical barrier load partition.

To summarize, we have clearly defined the cabin area where we want minimal deformation which may injure the occupants. It is the cabin area which we want to decelerate within the accelerations levels we have identified earlier. We also defined a crush zone which we expect to deform upon impact and which must generate the forces which decelerate the cabin zone in the desired manner. Now that we have targets for average and maximum allowable crush force, we can now size structural elements. Some of the elements in the crush zone are sized to provide forces as they crush, and other structural elements around the cabin zone are sized to ensure that area is not intruded upon, Figure 6.16. We now look at tools to aid in sizing both these classes of structural elements.

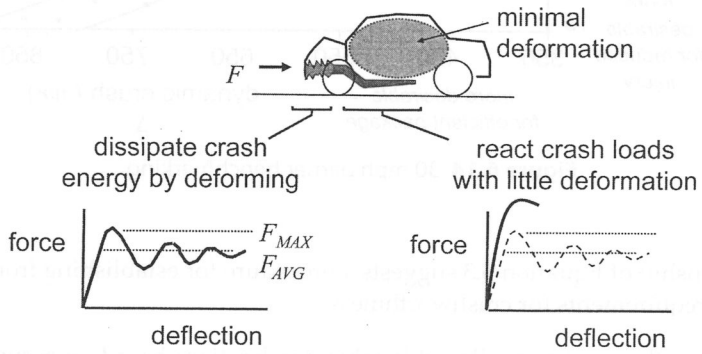

Figure 6.16 Structure requirements for front barrier.

6.2.3 Beam sizing for energy absorption

First let us consider the structural elements in the crush zone and focus on the major load path—the mid rail. Using the procedure of the previous section, we have identified the required average crush force, and also the maximum allowable force. An efficient means to generate an approximately square wave force over a large distance is through progressive column crush of a thin-walled section, Figure 6.17 [4]. In this figure we see a thin-walled square section undergoing an axial compressive load, F. For small loads, the column is under simple compressive stress, $\sigma=FA$, A being the cross-section area, Figure 6.17a. As the compressive load is gradually increased, the elastic buckling load for the section walls is reached and the

walls buckle, Figure 6.17b. As the load continues to increase past the ultimate load of the buckled walls, a load is reached where the corners of the section cripple and the load drops, Figure 6.17c. Once the crippled corner bottoms out, the load begins to increase again, Figure 6.17d. This process repeats itself, forming an accordion pattern and a load-deformation curve which oscillates about an average crush force, Figure 6.17e & f.

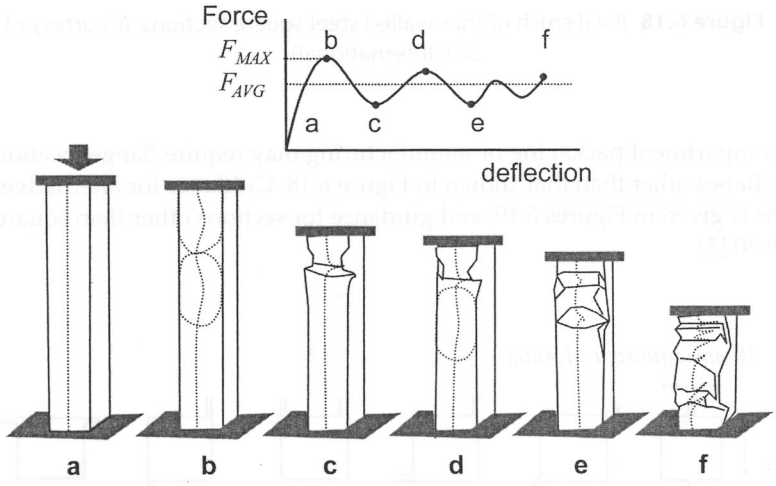

Figure 6.17 Square section under axial compressive load. (Courtesy of SAE International)

This physical behavior is very useful for energy absorption as it generates a high average crush force with a square wave character. An empirical relationship for predicting forces during crush, Figure 6.18, is given in Equation 6.4 [4]. Note that this relationship was developed for a square steel section loaded by static (very slowly applied) forces. The units are *N*, *mm*, N/mm^2.

$$\begin{aligned} P_M &= 386 t^{1.86} b^{0.14} \sigma_Y^{0.57} \\ P_{MAX} &= 2.87 P_M \\ P_1 &= 1.42 P_M \\ P_2 &= 0.57 P_M \end{aligned} \tag{6.4}$$

where:

P_M = Static mean crush force (*N*)

P_{MAX} = Maximum crush force (*N*)

P_1 and P_2 = crush loads shown in Figure 6.18 (*N*)

t = Material thickness (*mm*)

b = Section width and height (*mm*)

σ_Y = Material yield stress (N/mm_2)

Using Equation 6.4, we can determine the thickness, t, section width, w, and yield stress, σ_Y, to generate the required average static crush force.

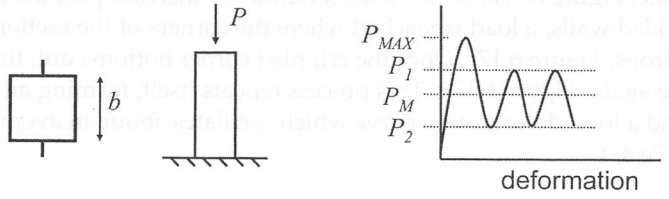

Figure 6.18 Axial crush of thin-walled steel square sections. (Courtesy of SAE International)

Motor compartment packaging or manufacturing may require flange locations and section shapes other than that shown in Figure 6.18. Guidance for alternative flange positions is given in Figures 6.19, and guidance for sections other than square in Figure 6.20 [5].

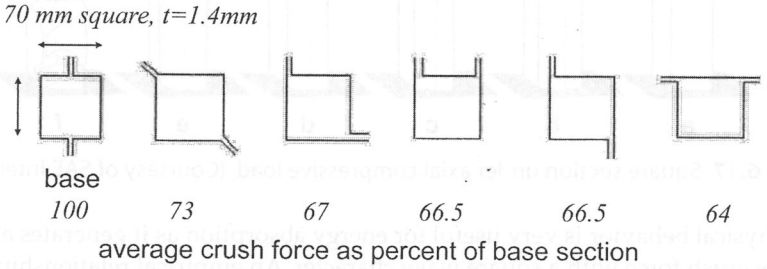

Figure 6.19 Flange position effect on average crush force. (Courtesy of the American Iron and Steel Institute, Automotive Steel Design Manual))

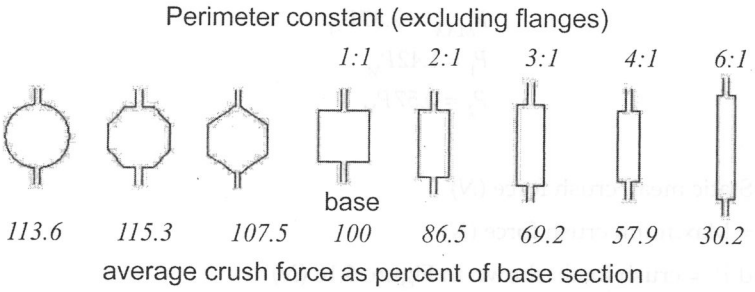

Figure 6.20 Section shape effect on average crush force. (Courtesy of the American Iron and Steel Institute, Automotive Steel Design Manual)

A final adjustment to Equation 6.4 is made for dynamic loading. Crush load requirements are load levels which must be generated during a *dynamic* impact in which the loading is done over a short time. Many materials are strain rate sensitive and generate higher stress when loaded rapidly (steel is one such material). Figure 6.21 compares the loads generated in both a static test along with the same section tested by impacting at *48 km/h (30 mph)* [5]. These data may be used to adjust the values predicted by Equation 6.4 to arrive at dynamic crush force. From Figures 6.20, the effectiveness of a polygon (Shapes B and C) is evident. Many contemporary designs apply this concept, Figure 6.22, and also use shape optimization to improve energy absorbed [6].

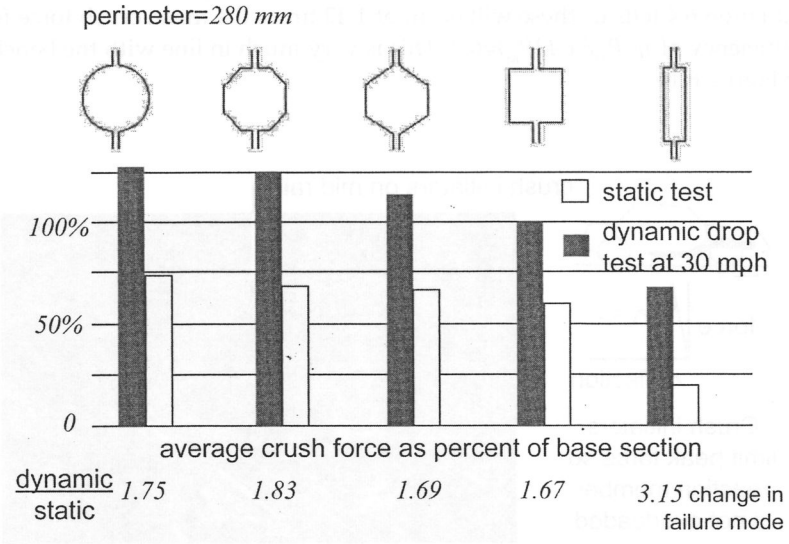

Figure 6.21 Dynamic effect on average crush force. (Courtesy of the American Iron and Steel Institute, Automotive Steel Design Manual)

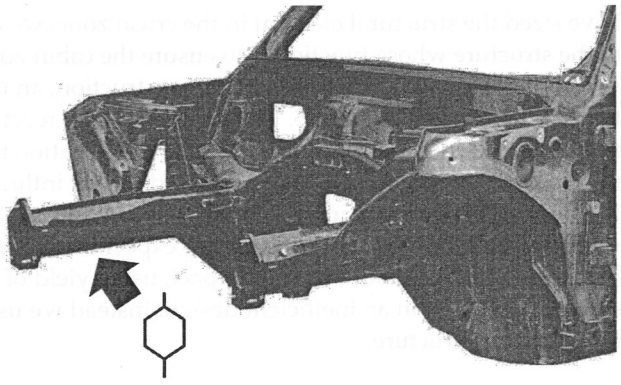

Figure 6.22 Use of hexagonal sections. (Photo courtesy of A2Mac1.com, Automotive Benchmarking)

Note that along with the mean crush force, P_M, Equation 6.4 predicts the maximum load, P_{MAX}, at 2.87 times the mean load. This is the load needed to initiate the first crippled corner. With this factor, the crush efficiency for an unmodified square section is:

$$\eta=F_{AVG}/F_{MAX}=P_M/(2.87P_M)=0.35$$

which is rather poor compared with the benchmark data from Figure 6.14. To improve this efficiency, we need to reduce the maximum load. Understanding that this load is caused by the initial corner crippling, darts or beads are often added to initiate the crippling, Figure 6.23. The precise placement and geometry of these *crush initiators* is found by simulation or experimentation. Once the initial crippling load has been reduced, we are left with the subsequent crippling cycles at load P_1, Figure 6.16. Equation 6.4 tells us these will occur at 1.42 times the mean crush force for a crush efficiency of $\eta=P_M/(1.42P_M)=0.7$. This is very much in line with the benchmark data of Figure 6.14.

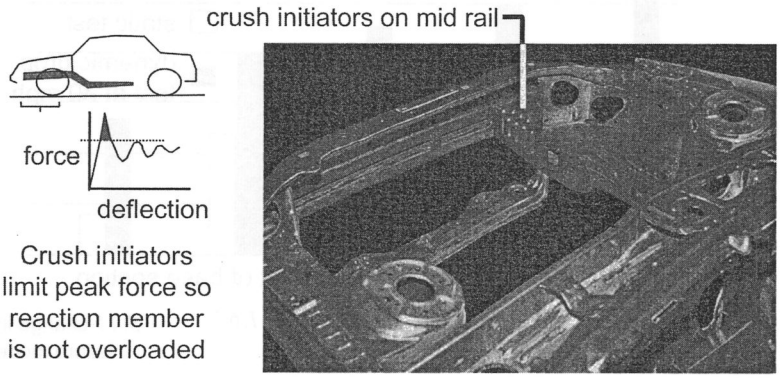

Figure 6.23 Crush initiators. (Photo courtesy of A2Mac1.com, Automotive Benchmarking)

6.2.4 Beam sizing for cabin reaction structure

Now that we have sized the structural element in the crush zone, we can turn our attention to the structure whose function is to ensure the cabin zone does not excessively deform, Figure 6.24. In typical body construction, an under-floor structure reacts the crush loads, Figure 6.25. This structure must react the maximum loads generated by the midrail, F_{MAX}, without excessive deformation into the cabin area. In this case *excessive* deformation is a level which does not influence occupant trajectory during impact and does not increase injury: approximately *50–120 mm (2–4.75 in.)* of deformation into the cabin zone. As we expect the reaction structure to permanently deform a small amount during impact, using yield of the outer fiber as failure criterion would result in an inefficient design. Instead we use the *limit analysis* to size the reaction structure.

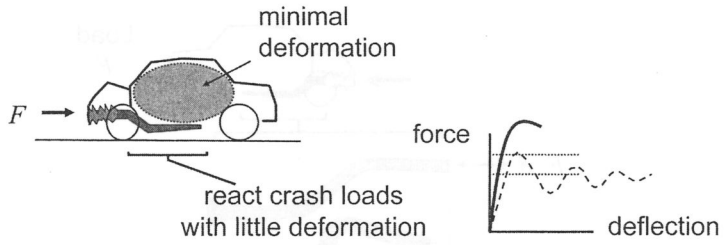

Figure 6.24 Reaction member requirements.

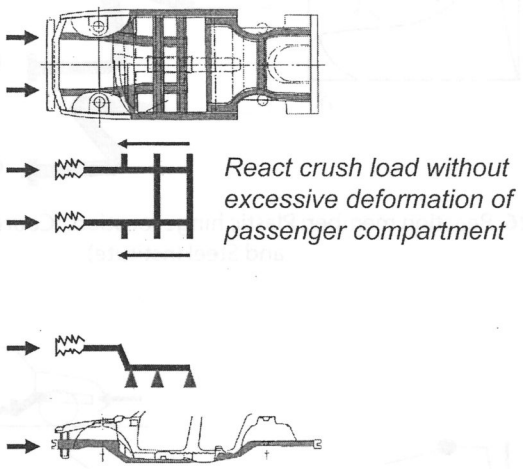

Figure 6.25 Maintaining integrity of the passenger compartment.

6.2.5 Limit analysis design

In *limit analysis* we look at a structure as reaching its load capacity just as it behaves as a mechanism with *plastic hinges*, Figure 6.26 [7, 8, 9, 10]. For example, in this structure we consider the horizontally applied load to be gradually increasing. Initially the reaction structure will react this load elastically; as the load is increased we will begin to see yielding in the areas shown. If we were designing a structure in which initiation of permanent deformation was the failure criterion, this state would indicate the failure load. However, for a reaction structure, we can continue to increase the applied load until the yield zones extend across the section at the two key locations shown in Figure 6.26. We define these locations to be plastic hinges. Continuing to increase the applied load beyond this point, load *A* in Figure 6.26, will cause the reaction structure to behave as a mechanism with rigid links connected at the plastic hinge locations, Figure 6.27. At this load, the structure will distort without bound. We define the limit load as the ultimate load-carrying ability for the structure. We will analyze this behavior using the model shown in Figure 6.27. Here we view the structure as consisting of rigid links and ideally plastic hinges. Before we do an analysis to predict the limit load for a particular structure, let us look closer at the behavior of an individual plastic hinge.

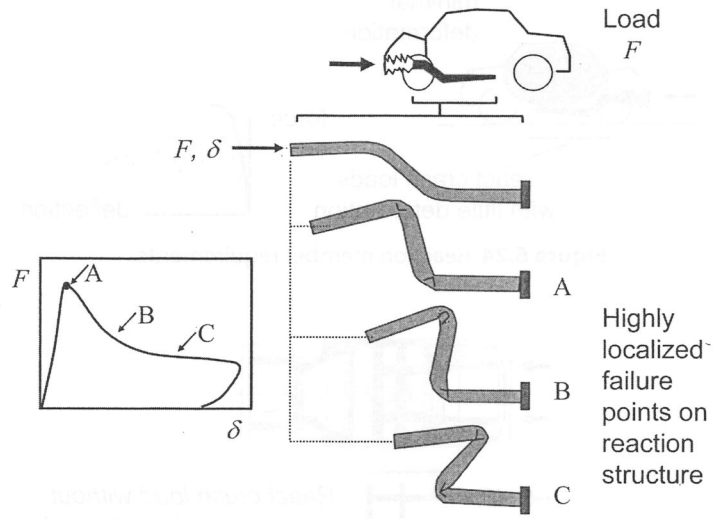

Figure 6.26 Reaction member: Plastic hinge location. (Courtesy of the American Iron and Steel Institute)

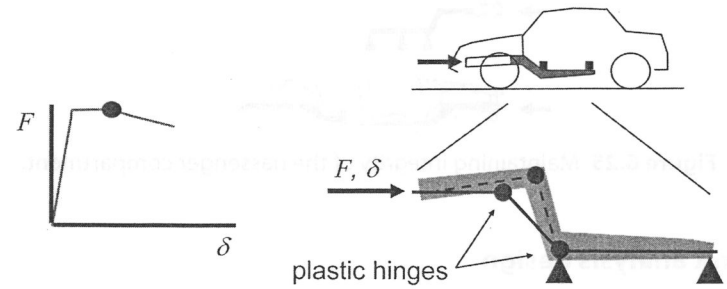

Figure 6.27 Limit analysis of structures.

6.2.6 Plastic hinge behavior

Consider a simple plastic hinge, Figure 6.28 [11]. Here a cantilever beam has a vertical tip load. Focus on the stresses at the section next to the wall. With s mall applied loads, the stress distribution is linear and elastic, condition *a* in Figure 6.28. Releasing the load in this range will result in a return to the original shape. This behavior is shown in the load-deflection curve, Figure 6.28a. As the load is increased, a load is reached where the outer fiber of the section reaches yield, condition *b*. If we continue loading a small amount above this load and then release the load, the beam will show some permanent deformation. However, we have not reached the maximum or ultimate load which the beam can react. Continuing to increase the tip load, the yielded (plastic) region will continue to increase toward the middle of the section with the stress distribution being shown in Figure 6.28c. The ultimate load-carrying capacity of the beam has even now not yet been met.

Eventually the whole section is in a state of yield with compressive yield stress on the lower part of the section and tensile yield stress on the upper part of the section, Figure 6.28d. At this load the yielded section acts like a pinned joint with a resisting moment—like a rusty gate hinge. Once we have reached this load, the beam will continue to deflect without bound in the manner of a rigid bar pinned at the wall. This defines the limit load—the ultimate load-carrying capacity of this structure.

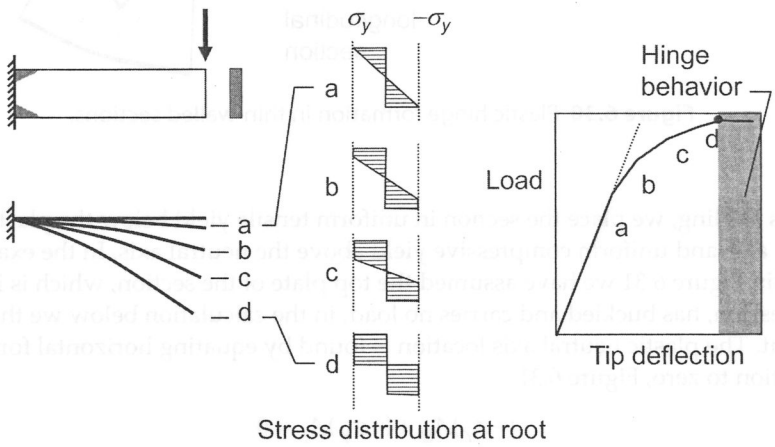

Figure 6.28 Limit analysis example: Cantilever beam.

We can model a plastic hinge as shown in Figure 6.29 as a pinned joint with a uniform resisting moment, M_p throughout the range of angular deformation. The value for M_p depends on the section dimensions and material yield stress [12]. To arrive at a value for M_p, consider the physical behavior of a square thin-walled section shown in Figure 6.30.

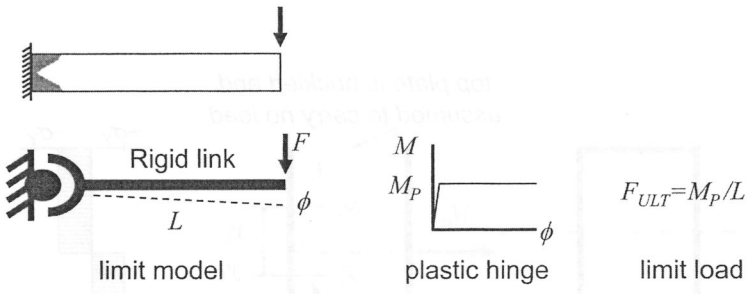

Figure 6.29 Plastic hinge first-order model.

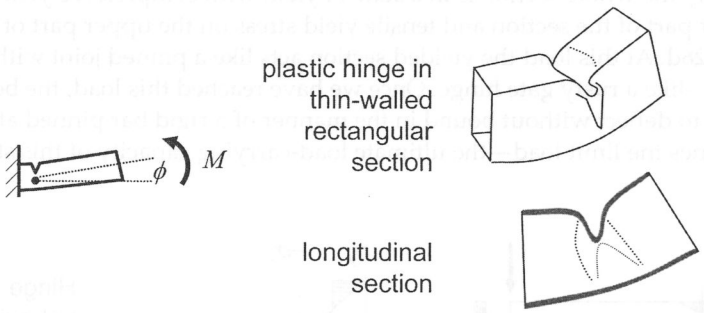

Figure 6.30 Plastic hinge formation in thin-walled sections.

For this loading, we place the section in uniform tensile yield below the plastic neutral axis and uniform compressive yield above the neutral axis. In the example shown in Figure 6.31 we have assumed the top plate of the section, which is in compression, has buckled and carries no load; in the calculation below we therefore ignore it. The plastic neutral axis location is found by equating horizontal force on the section to zero, Figure 6.31.

$$(-\sigma_Y)A_U + (+\sigma_Y)A_L = 0$$
$$A_U = A_L$$

where:

A_U = Cross section area above the plastic neutral axis

A_L = Cross section area below the plastic neutral axis

σ_Y = Material yield stress

The plastic neutral axis location is then defined as the axis where the area above and below are equal. (Note that the elastic and plastic neutral axes are not necessarily the same.)

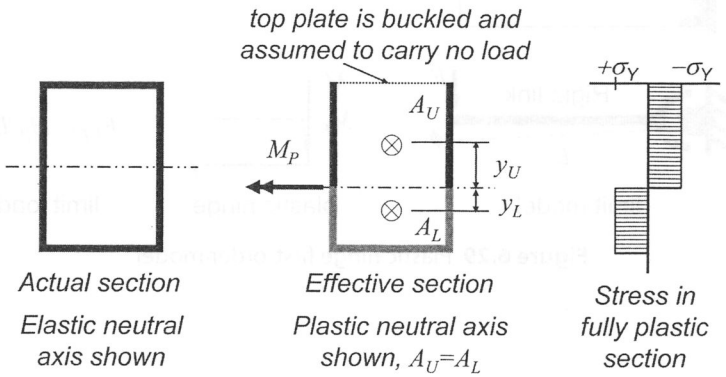

Figure 6.31 Example: Calculating M_P

The plastic moment, M_P, is now found by summing moments about the plastic neutral axis, Figure 6.31. This result is given by

$$M_P = \sigma_Y (A_U y_U + A_L y_L) \tag{6.5}$$

where:

M_P = Plastic moment

A_U = Cross section area above the plastic neutral axis

A_L = Cross section area below the plastic neutral axis

y_U = Distance from the plastic neutral axis to the center of area for the upper area, A_U

y_L is the distance from the plastic neutral axis to the center of area for the lower area, A_L

σ_Y = Material yield stress

To better understand design principles for an effective plastic hinge, consider a square section shown in Figure 6.32. We calculate the moment for three cases: a) the moment which causes the yield of the outermost fiber, b) the moment for the fully plastic state when all elements of the section are fully effective, and c) the moment in the fully plastic state when the compression element of the section has buckled and carries no load. Figure 6.33 shows the values for these moments identified on the moment-angular deflection curve for the beam. To provide the highest load reaction capability, we would like the plastic hinge to follow *Curve A*. However, if elements of the section buckle before yield, the path will be *Curve C*. If buckling occurs after yield, the path will be *Curve B*—both *B* and *C* being less effective than *Curve A*. To obtain *Curve A*, we must inhibit buckling of the compression element even beyond the yield stress. Figure 6.34 illustrates an approach to achieve this using section reinforcement.

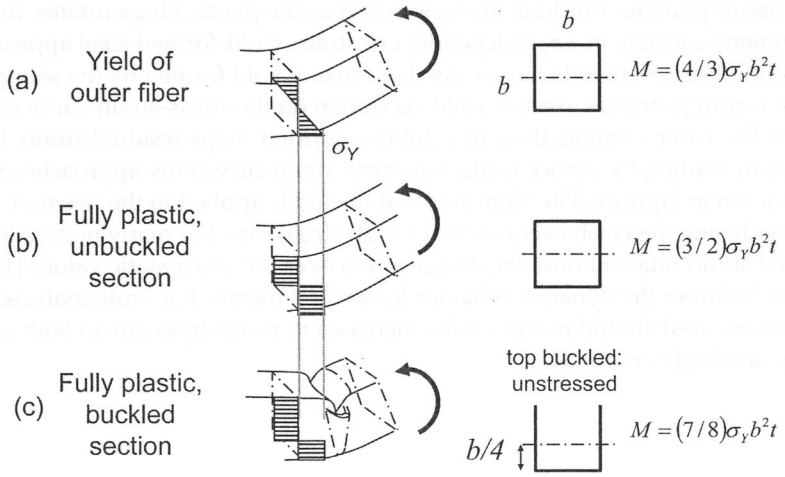

Figure 6.32 Plastic hinge example: square thin-walled section.

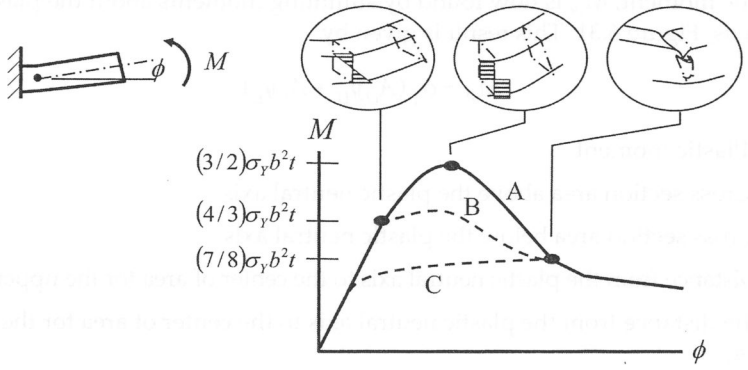

Figure 6.33 Plastic hinge behavior.

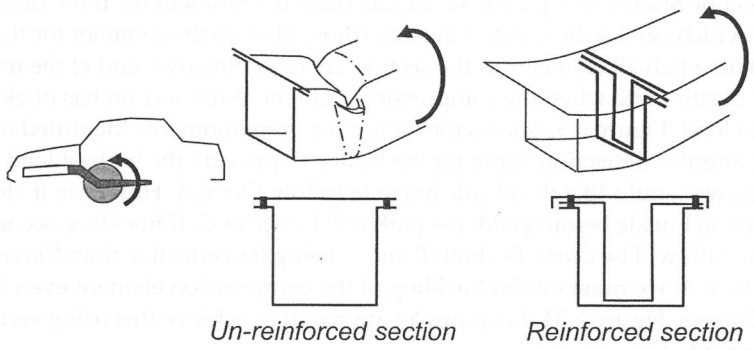

Figure 6.34 Reinforcement to increase plastic moment capacity.

A final assumption for our limit analysis is that as the plastic hinge rotates, the stress level remains constant at $\pm\sigma_Y$ independent of strain. Cold-formed steel approaches this assumed stress-strain behavior. As sheet steel is cold formed by the stamping process, forming stresses exceeds yield, as shown on the stress-strain curve of Figure 6.35a. After forming, the part exhibits a formed shape residual strain. Upon subsequent loading by service loads, the stress-strain curve now approaches the shape shown in Figure 6.35b. Note also that the loads applied to the reaction structure during the crash event induce a high strain rate. For many materials, this increased strain rate will raise the design stress over the quasi-static values [13, 14]. Figure 6.36 shows the dynamic behavior for several metals. For limit analysis, the design stress used should recognize the increases to yield stress due to both cold forming and high strain rate.

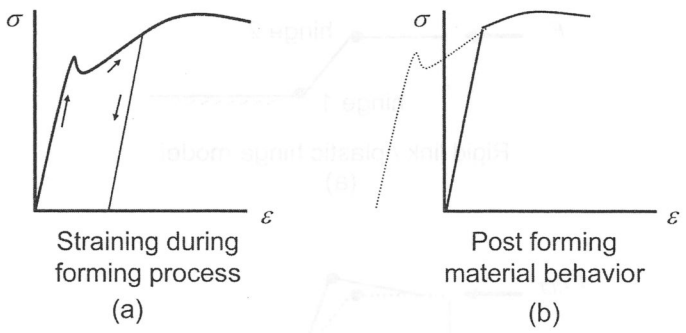

Figure 6.35 Work hardening.

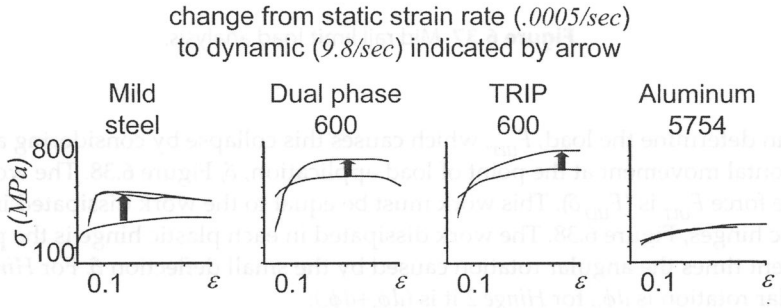

Figure 6.36 Dynamic stress-strain behavior.

Now that we have a means to estimate the plastic moment for a specific section, we can apply limit analysis to the cabin structure. Our objective is to identify the limit load capacity of the cabin structure and ensure it is sufficient to react the crush loads being generated by the midrail structure during crush. A typical design for cabin structure is shown in Figure 6.37. This longitudinal structure connects to the crushable midrail and extends down along the toe pan and under the passenger compartment. It is supported under the passenger compartment by cross members extending out to the rocker beams and is also supported by the floor pan in shear.

We can isolate the longitudinal structure, restrain it at the floor pan connection, and load it with a horizontal force representing the crush load being applied, Figure 6.37a. Applying limit analysis concepts, we view this structure as two rigid beams connected by two plastic hinges. The applied load, F_{ULT}, which induces this state, is the ultimate load for this structure. Attempts to exceed this load will cause the structure to collapse by rotations about the hinges as shown in Figure 6.37b.

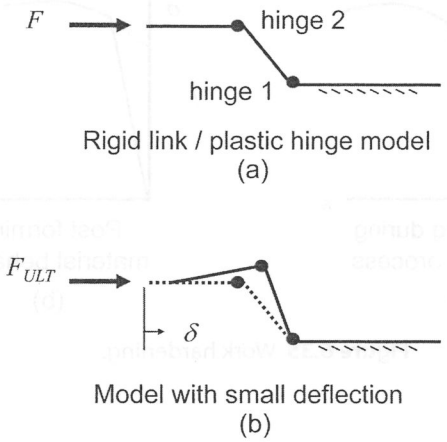

Figure 6.37 Mid rail limit load analysis.

We can determine the load, F_{ULT}, which causes this collapse by considering a small horizontal movement at the point of load application, δ, Figure 6.38. The work done by the force F_{ULT} is $(F_{ULT}\delta)$. This work must be equal to the work dissipated in the plastic hinges, Figure 6.38. The work dissipated in each plastic hinge is the plastic moment times the angular rotation caused by the small deflection δ. For *Hinge 1* this angular rotation is $d\phi_1$, for *Hinge 2* it is $(d\phi_1+d\phi_2)$:

$$F_{ULT}\delta = M_{P1}d\phi_1 + M_{P2}(d\phi_1 + d\phi_2)$$

where:

$d\phi_1$ and $d\phi_2$ = Angular rotations

M_{P1} and M_{P2} = Plastic moments for each hinge

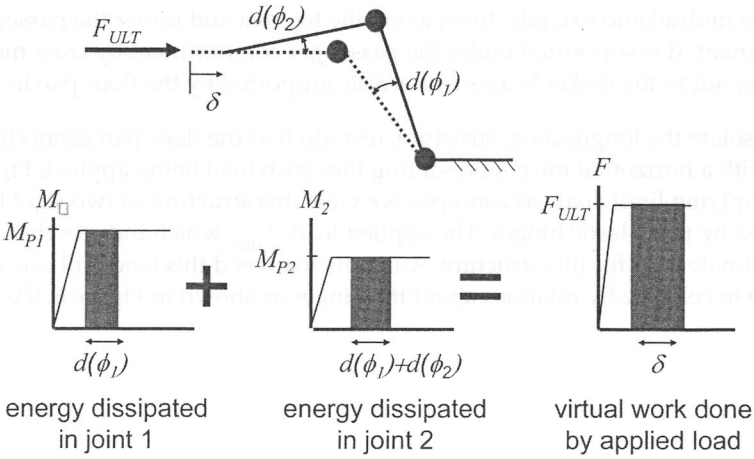

Figure 6.38 Work relationship for plastic hinge deformation.

The mechanism formed by this collapsing structure is kinematically deterministic. That is, knowing the deflection δ, we can calculate values for the angles of rotation, $d\phi_1$ and $d\phi_2$, using geometric relationships, Figure 6.39,

$$d\phi_1 = \frac{\delta}{L_1 \sin(\phi_1)}, \qquad d\phi_2 = \frac{\cos(\phi_1)\delta}{L_2 \sin(\phi_1)}$$

Substituting these angles into the above work balance yields,

$$F_{ULT}\delta = M_{P1}d\phi_1 + M_{P2}(d\phi_1 + d\phi_2)$$

$$F_{ULT}\delta = M_{P1}\left(\frac{\delta}{L_1 \sin(\phi_1)}\right) + M_{P2}\left(\frac{\delta}{L_1 \sin(\phi_1)} + \frac{\cos(\phi_1)\delta}{L_2 \sin(\phi_1)}\right)$$

$$F_{ULT} = M_{P1}\left(\frac{1}{L_1 \sin(\phi_1)}\right) + M_{P2}\left(\frac{1}{L_1 \sin(\phi_1)} + \frac{\cos(\phi_1)}{L_2 \sin(\phi_1)}\right) \tag{6.6}$$

Thus knowing the geometry of the longitudinal structure (L_1, L_2, and ϕ_1) and the plastic moment capacity at the hinge joints (M_{P1} and M_{P2}), we can determine the load capacity, F_{ULT}, for the structure and ensure that it is large enough to react the crush loads.

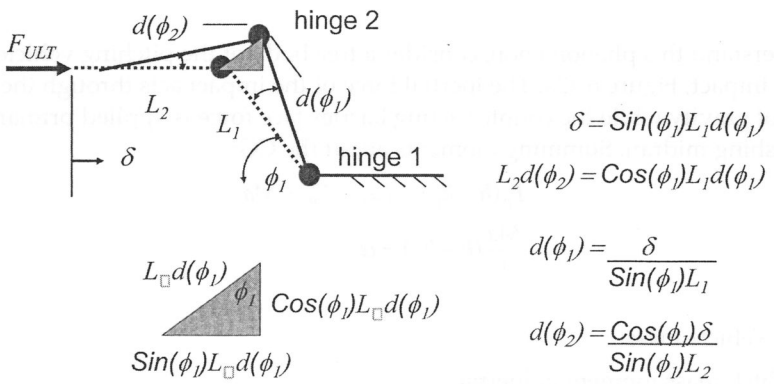

Figure 6.39 Geometric relationships.

6.2.7 Design for reducing vehicle pitch during impact

It has been observed that upon impact with a fixed barrier, some vehicles rotate in the side view with the rear raising upward, Figure 6.40. This rotation or pitch can increase the likelihood of neck injuries, Figure 6.41.

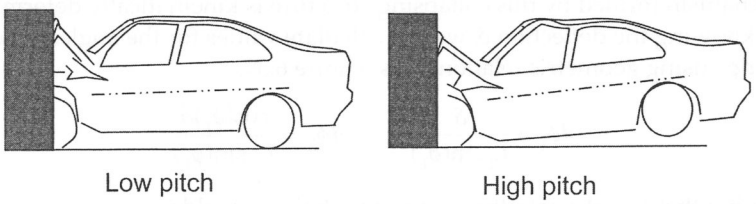

Figure 6.40 Vehicle pitch upon impact with rigid barrier

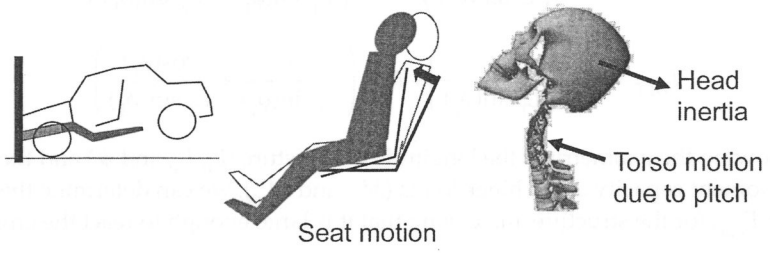

Figure 6.41 Neck injury related to vehicle pitch

To understand this phenomenon, consider a free body of the pitching vehicle at the time of impact, Figure 6.42a. The inertial force of the impact acts through the vehicle center of gravity while the counter-acting barrier face force is applied primarily at the crushing midrail. Summing moments about the CG:

$$F_B(h - h_L) = I\alpha, \quad F_B = Ma$$

$$\frac{Ma}{I}(h - h_L) = \alpha$$

where:

M = Vehicle mass

I = Pitch mass moment of inertia

h = Height of the CG above ground

h_L = Height of the effective load path above ground

α = Pitch acceleration

a = Acceleration of the vehicle during impact

In practice, the CG height is above the bumper height where the midrail is located. The difference in the heights of these equal and opposite forces creates a couple which causes the rotational (pitching) acceleration.

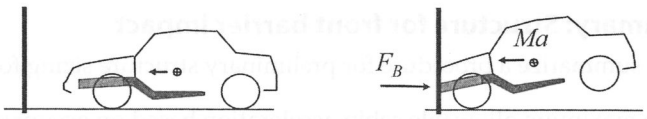

(a) Vehicle pitch without upper load path

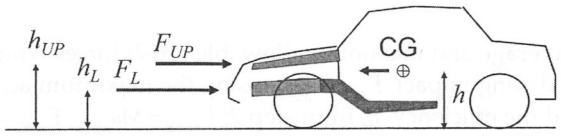

(b) Addition of upper load path

Figure 6.42 Reducing pitch upon impact.

To reduce pitching, we can add another crushable load path above the CG such that the moments about the vehicle CG for the two crushable load paths sum to zero, Figure 6.42b.

$$F_{UP}(h_{UP}-h)-F_L(h-h_L)=0$$
$$\frac{F_{UP}}{F_L}=\frac{h-h_L}{h_{UP}-h} \tag{6.7}$$

where:

F_{UP} = Average crush load generated by the upper load path

F_L = Average crush load generated by the lower load path

h = Height of the CG above ground

h_L = Height of the lower load path above ground

h_{UP} = Height of the upper load path above ground

In practice, the upper load path is just under the hood, and to the sides of the motor compartment, Figure 6.43.

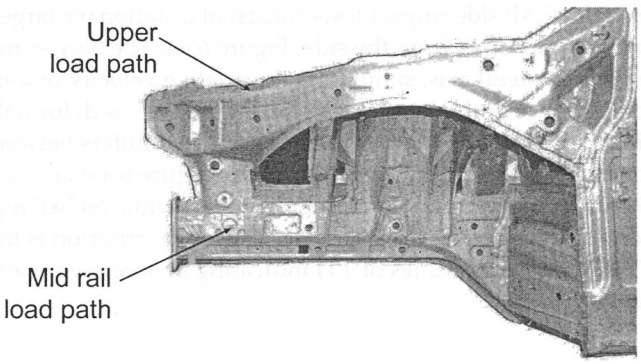

Figure 6.43 Example of upper load path. (Photo courtesey of A2Mac1.com, Automotive Benchmarking)

6.2.8 Summary: Structure for front barrier impact

We can now summarize a procedure for preliminary structure sizing for front impact:

1. Select the maximum allowable cabin acceleration based on occupant injury, a_{MAX}
2. Determine a consistent structural efficiency and crush space, (η, Δ, using Equation 6.3
3. Compute the average and maximum allowable crush forces which the vehicle must generate during impact, F_{AVG}, F_{MAX}, using the maximum acceleration, a_{MAX}, from step 1 and the efficiency, η, from step 2; $F_{MAX}=Ma_{MAX}$, $F_{AVG}=\eta F_{MAX}$
4. Allocate these total forces from step 3 to the structural elements within the vehicle front end, Figure 6.15
5. Size the crushable midrail using the average required crush force requirement of step 4 using Equation 6.4 and Figures 6.19–21
6. If the peak crush load, P_{MAX}, calculated in step 5 exceeds the maximum load requirement from step 4, then consider crush-initiator designs, Figure 6.23
7. The cabin reaction structure capacity must exceed the maximum midrail crush load identified in step 6. Use limit analysis to determine the required plastic moments for the hinges, Equation 6.6
8. Size the reaction structure sections to generate the hinge moments from step 7

Note that the structural requirements flow from vehicle requirements, and any change at the vehicle level must be examined for changes to the structural requirements.

6.3 Side Impact

Side impact plays an important role in sizing vehicle structure. As the strategy for side impact is quite different from that of front impact, this section is devoted to design for side impact. We will first look at the standardized vehicle tests and then flow down the vehicle level requirements to specific body structural elements.

Current FMVSS and NCAP side-impact tests consist of a stationary target vehicle and a moving barrier impacting from the side, Figure 6.44. The barrier moves at a 27° angle to the vehicle lateral axis, simulating the relative velocity of a side impact at an intersection. The face of the moving barrier, Figure 6.45, is deformable and crushes at a uniform *45 psi (0.31 N/mm²)*. The impact speed differs between FMVSS, *33.5 mph (53.6 km/h)*, and NCAP, *38.5 mph (61.6 km/h)* (Figure 6.46) and, as with front impact, FMVSS requires a minimum injury performance while NCAP reports the probability of serious injury using the star scale. The injury criterion is the Thoracic Trauma Index, TTI, with larger values of TTI indicating a more severe injury (a TTI<57 is desirable).

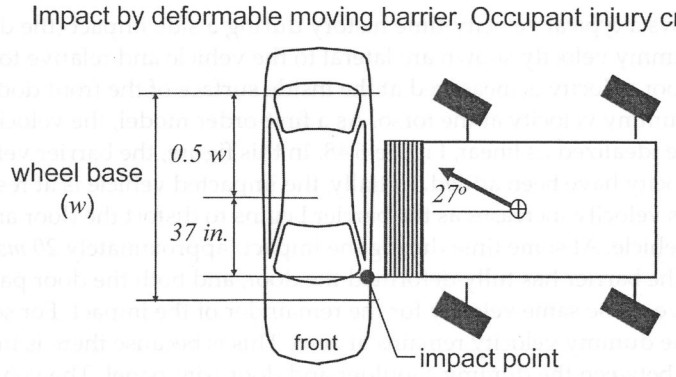

Figure 6.44 Side-impact test.

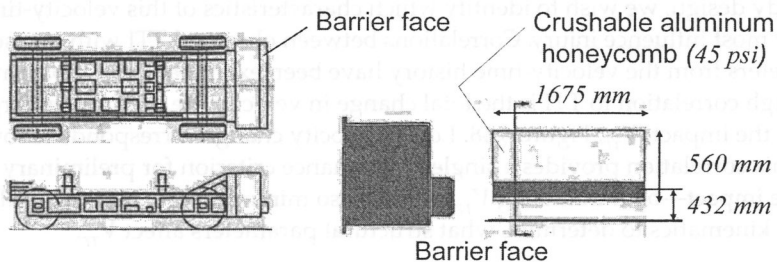

Figure 6.45 Rear moving barrier.

The SINCAP or LINCAP is based on the thoracic trauma index (TTI) using the US-SID dummy. TTI is defined as the average of the peak accelerations in the rib and lower spine.

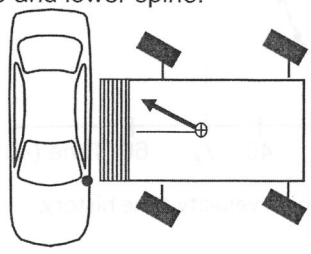

38.5 mph (61.6 km/h) impacted by *1370 kg* barrier moving *27°* to lateral axis of vehicle

Star Rating	% chance of serious injury
★★★★★	<5%
★★★★	6-10
★★★	11-20
★★	21-25
★	>26

Figure 6.46 Side impact: New car assessment program.

Figure 6.47 shows a typical velocity-time history during a side impact (the door velocity and dummy velocity shown are lateral to the vehicle and relative to ground). The door velocity is measured at the inside surface of the front door structure and dummy velocity at the torso. As a first-order model, the velocity-time histories may be idealized as linear, Figure 6.48. In this figure, the barrier velocity and vehicle velocity have been added. Initially, the impacted vehicle is at rest with zero velocity. Its velocity increases as the barrier begins to distort the door and accelerate the vehicle. At some time during the impact (approximately *20 msec* in Figure 6.48) the barrier has fully deformed the door, and both the door panel and barrier move at the same velocity for the remainder of the impact. For several milliseconds, the dummy velocity remains at zero. This is because there is initially some clearance between the dummy shoulder and door trim panel. The vehicle must slide laterally through this distance before the dummy is struck (this occurs at approximately *25 msec*). The dummy is then accelerated by the door trim panel until both the door and dummy reach the same speed (*~50 msec*). The dummy impact event is over at this time, T_{FINAL}.

For body design, we wish to identify which characteristics of this velocity-time history most influence injury. Correlations between observed TTI with measured parameters from the velocity-time history have been examined [15]. A parameter with high correlation to TTI is the total change in velocity the dummy undergoes during the impact, V_{TF}, Figure 6.48. Lower velocity change corresponds to lower TTI. This correlation provides a single performance criterion for preliminary design for side impact—by minimizing V_{TF} we will also minimize TTI. We now analyze impact kinematics to determine what structural parameters affect V_{TF}.

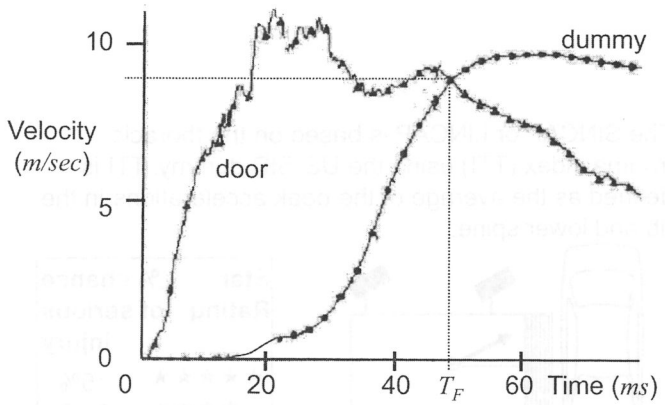

Figure 6.47 Side-impact velocity-time history.

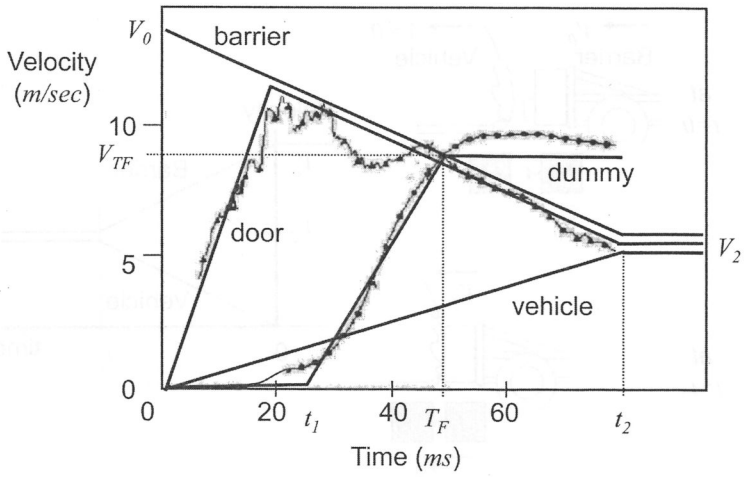

Figure 6.48 Idealized side-impact velocity-time history.

6.3.1 Kinematic and load path analysis of side impact

Consider the impact of the vehicle by a moving barrier [16]. We can model each as a point mass with the impact being perfectly plastic, Figure 6.49. In this linear model, we are looking at motions lateral to the vehicle and will consider the lateral component of the barrier velocity as the initial impact velocity, $V_0 = S_{TEST} \cos \alpha$, where S_{TEST} is the standard test impact speed and α is the angle of impact. As no external forces are applied to the impacting masses, the momentum is unchanged before and after the impact. Equating the momentum yields a relationship for final velocity, V_2.

$$M_1(V_0) = (M_1 + M_2)V_2$$

$$V_2 = \frac{M_1}{M_1 + M_2} V_0 \tag{6.8}$$

where:

M_1 = Barrier mass

M_2 = Vehicle mass

V_0 = Lateral impact speed

V_2 = Final speed of vehicle and barrier

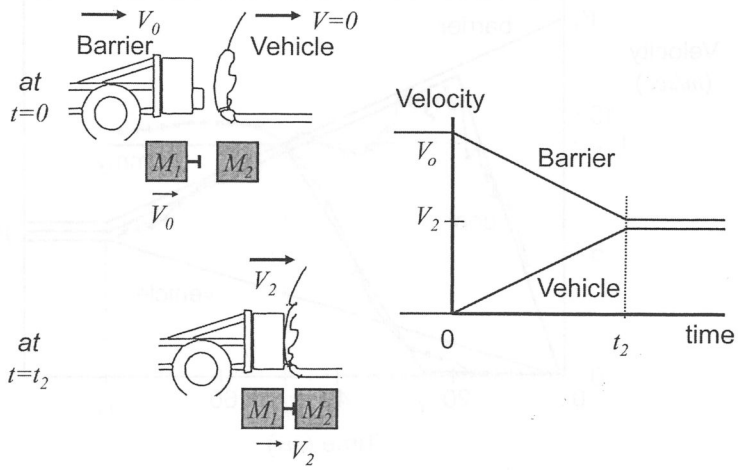

Figure 6.49 Terminal velocity in side impact.

We now idealize the crush characteristics of the side of the vehicle by assuming a square wave for crush load vs. lateral deformation, Figure 6.50. By looking at a free body of each mass during impact, we can find the acceleration during impact for each mass:

$$-F_2 = M_1(a_1), \quad F_2 = M_2(a_2)$$

$$a_1 = \frac{-F_2}{M_1}, \quad a_2 = \frac{F_2}{M_2} \tag{6.9}$$

where:

a_1 = Barrier acceleration

a_2 = Vehicle lateral acceleration

F_2 = Crush load for the vehicle side (note: $F_2 \geq 290{,}000$ *N (65,200 lb)*, the moving barrier face crush capacity)

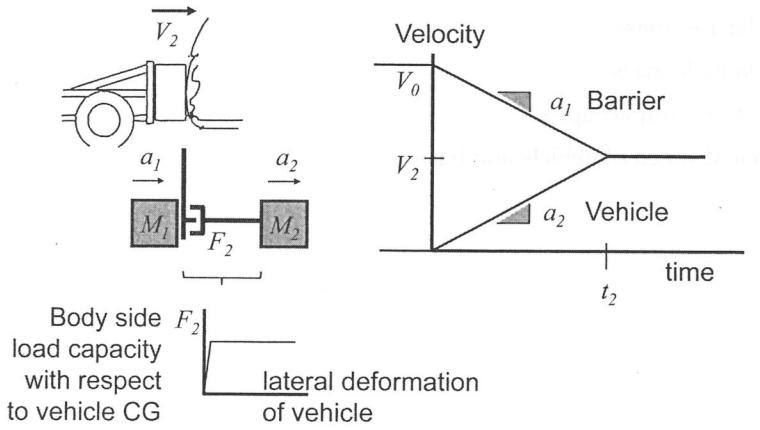

Figure 6.50 Vehicle and barrier acceleration in side impact.

The time for the impact event, t_2, can be found by equating the time it takes to accelerate the vehicle to V_2

$$a_2 t_2 = V_2$$

$$t_2 = \frac{V_2}{a_2} \tag{6.10}$$

where t_2 = Time at the end of the impact event

We can now sketch the velocity-time histories for the barrier and vehicle center of gravity in this idealized model, Figure 6.50.

Remember that the area under the velocity-time history is the distance traveled relative to ground, Figure 6.51.

$$\text{distance traveled} = \int_0^{t_f} V dt$$

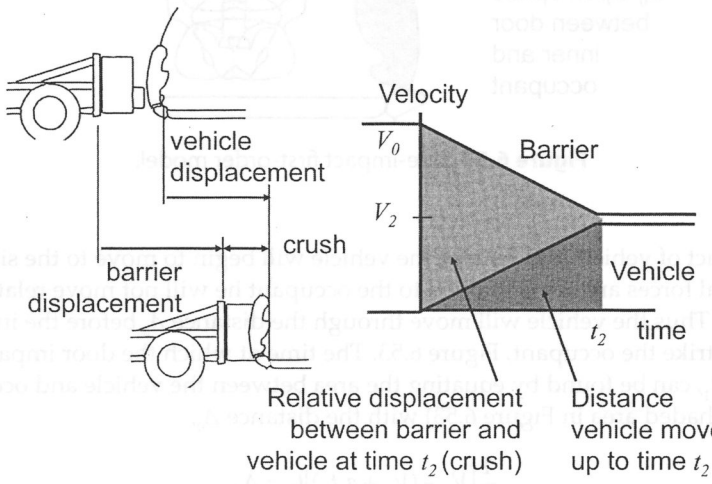

Figure 6.51 Relative crush in side impact.

Thus the area under the *vehicle v-t* graph up to time t_f is the distance the vehicle slides laterally; and the area under the *barrier v-t* graph is the distance it slides. By looking at the area between the two graphs up to time t_2 we find the difference of these two distances or the relative crush of the vehicle and barrier during impact, Figure 6.51. From the geometry of the curve, this crush is

$$crush = \frac{1}{2} V_0 t_2$$

Now we can turn our attention to the interior of the vehicle and the impact between occupant and door. We imagine the occupant sitting on the vehicle mass, but not

restrained in the lateral direction, Figure 6.52. We now add a mass-less rigid door side to the outer end of the vehicle crush element, F_2. To this door outer side, we add a crush element at the occupant shoulder level which represents the crush characteristics of the door and trim panel, Figure 6.52. There is a space, Δ_0, between the inside of the door crush element and occupant shoulder, and a door width of Δ.

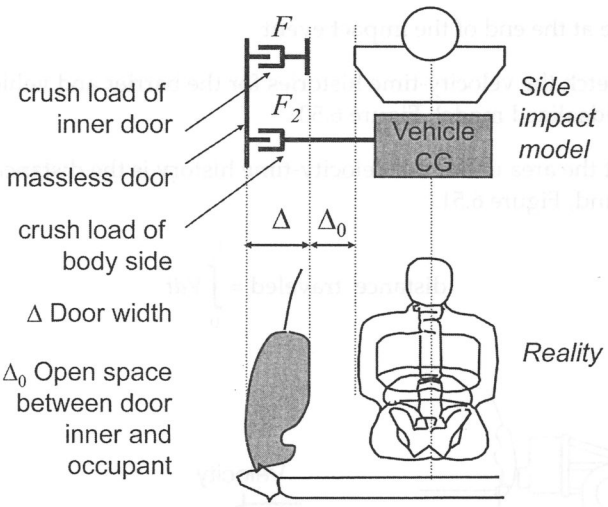

Figure 6.52 Side-impact first-order model.

Upon impact of vehicle and barrier, the vehicle will begin to move to the side, but as no lateral forces are being applied to the occupant he will not move relative to ground. Thus the vehicle will move through the distance Δ_0 before the inner door will strike the occupant, Figure 6.53. The time at which the door impacts the occupant, t_1, can be found by equating the area between the vehicle and occupant v-t histories (shaded area in Figure 6.53) with the distance Δ_0,

$$\frac{1}{2}\left[V_0 + (V_0 + a_1 t_1)\right] t_1 = \Delta_0$$

$$t_1^2 + \frac{2V_0}{a_1} t_1 - \frac{2\Delta_0}{a_1} = 0$$

using the quadratic formula:

$$t_1 = \frac{-\frac{2V_0}{a_1} \pm \sqrt{\left(\frac{2V_0}{a_1}\right)^2 + 4\left(\frac{2\Delta_0}{a_1}\right)}}{2} \tag{6.11}$$

where t_1 = Time at which the occupant begins to strike door.

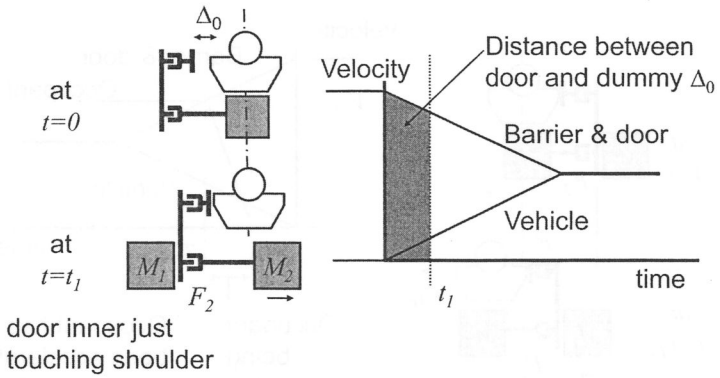

Figure 6.53 Time at occupant impact.

At this time, the door side begins to load the occupant with force and to accelerate him to the side.

The door side now accelerates the occupant laterally, Figure 6.54. Once the velocity of the door and occupant are equal, there will be no more relative deformation between the two, and the impact between the door and occupant is over. This occurs when the door inner has crushed through a distance of Δ. We equate the area under the occupant velocity history between the time t_1 and time T_F (the shaded area in Figure 6.55) with the door crush, Δ.

$$\frac{1}{2}\left[T_F - t_1)\right]V_1 = \Delta$$

where V_1 = Velocity at time t_1:

$$V_1 = V_0 + a_1 t_1 \tag{6.12a}$$

$$T_F = \frac{2\Delta}{V_1} + t_1 \tag{6.12b}$$

where T_F = Time at which the occupant and door are moving at same speed

Our objective for this kinematic analysis was to estimate the change in velocity of the occupant, V_{TF} as an indicator of injury. We can now estimate this change in velocity,

$$V_{TF} = V_0 + a_1 T_F \tag{6.13}$$

where V_{TF} = Velocity change of occupant from initial contact with the interior to release

We can also estimate the occupant acceleration as

$$a_{OCC} = \frac{V_{TF}}{T_F - t_1} \tag{6.14}$$

where a_{OCC} = Average acceleration of occupant during contact with the interior

This acceleration represents a minimum value and assumes the deformation characteristic of the door inner has a square wave load-deformation crush curve.

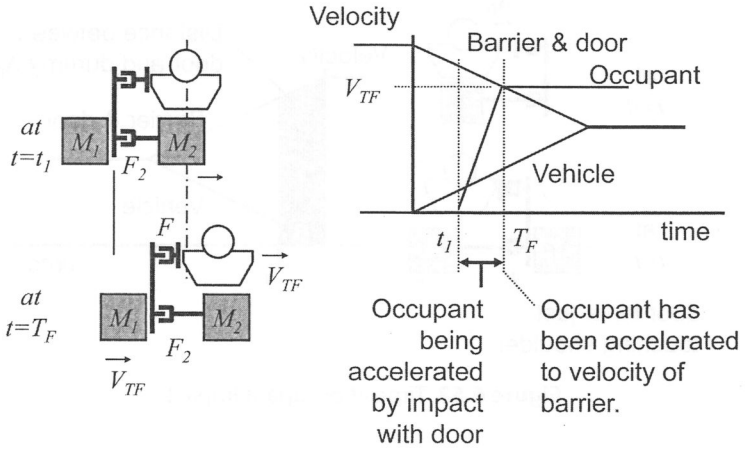

Figure 6.54 Occupant acceleration.

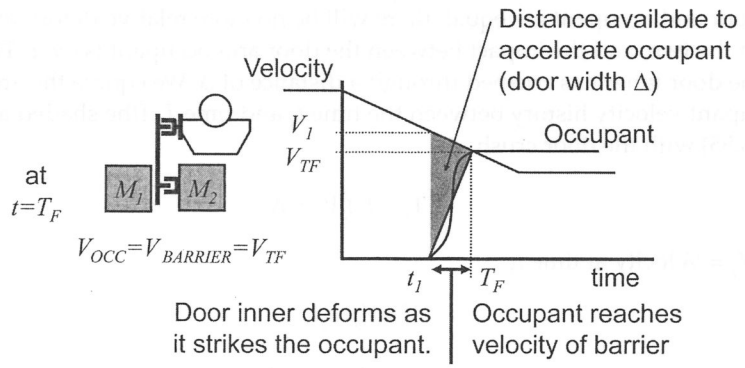

Figure 6.55 Body door inner deformation characteristics.

We can now completely define the velocity-time histories using the above equations, Figure 6.56, when given the impact speed, V_0; the barrier and vehicle masses, M_1 and M_2; the force characteristics for the body side, F_2; and the dimensions for the door crush thickness and space between occupant and door inner, Δ and Δ_O.

Remember that occupant injury in a side impact is correlated with the total velocity change for the occupant, V_{TF}, and reducing V_{TF} reduces occupant injury.

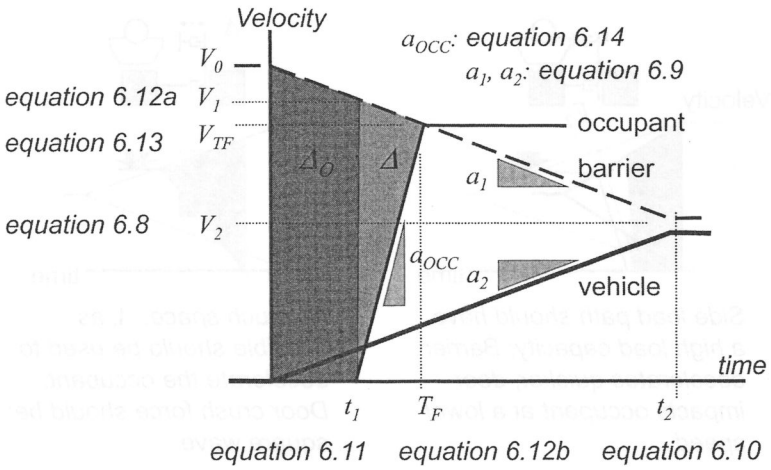

Figure 6.56 Summary of kinematic relationships.

6.3.2 Flow down of requirements for side impact

Using the kinematic relationships derived, we can now look at the influences on V_{TF} for three structural parameters.

Crush load for the vehicle side

The body side crush load, F_2, should be high. Increased side crush force decelerates the barrier quickly before impact with the occupant, Figure 6.57a. Thus the occupant is struck by the door at a lower velocity. Physically this high side crush force can be achieved with rigid side-to-side structural members aligned at the barrier face height. A cross member at the B pillar location or at the front of the rear seat pan is effective. Also, the barrier face must be engaged early by aligning structural members such as the rocker, lower B, and C pillars at the height of the barrier face.

Clearance between the occupant shoulder and door panel

It is desirable to use the space between the occupant and door outer surface, Δ, to minimize the impact acceleration of the occupant. Increasing this space decreases the average slope of the occupant velocity curve, Figure 6.57b, and results in a lower door impact force being applied to the occupant.

Door inner crush characteristic

When the door crush characteristic, F, is a square wave, the peak acceleration of the occupant is minimized, Figure 6.55. A means to accomplish this is by using crushable foam placed in the door trim area.

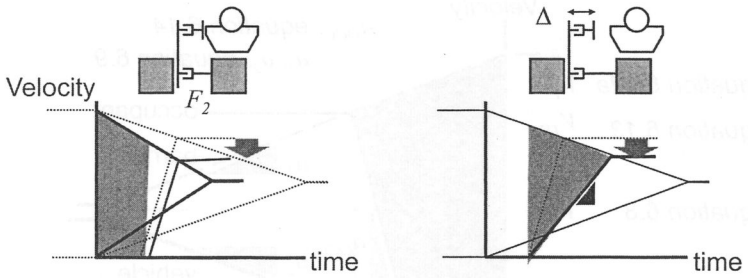

Side load path should have a high load capacity; Barrier decelerates quicker, door impacts occupant at a lower speed.

(a) Body side load path characteristic

As much space, Δ, as possible should be used to decelerate the occupant. Door crush force should be square wave

(b) Occupant to door space allocation

Figure 6.57 Desirable design parameters for side impact.

6.4 Note on Rear Impact

In the standard rear impact test, the stationary target vehicle is impacted by a moving barrier, Figure 6.58. The criterion for this test is to minimize fuel system leakage, so we are interested in absorbing the energy of the barrier by deforming structure rearward of the fuel system. If we could replace this impact with one between a moving vehicle and fixed barrier, we could apply the structure-sizing procedure developed for the front barrier case. To do this, we must identify the equivalent impact velocity which would result in the same work of deformation to be done by the structure.

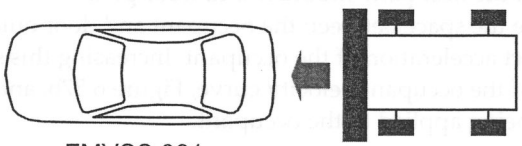

FMVSS 301

30 mph Impact by moving barrier

Fuel system integrity

Figure 6.58 Rear barrier.

We first apply conservation of momentum principles to find the final moving barrier impact speed, Figure 6.59a & b.

$$M_1(0) + M_2 V_0 = (M_1 + M_2) V_F$$

$$V_F = \frac{M_2}{M_1 + M_2} V_0$$

where:

M_1 = Struck vehicle mass

M_2 = Moving barrier mass

V_0 = Initial moving barrier speed

V_F = Common final speed of vehicle and barrier

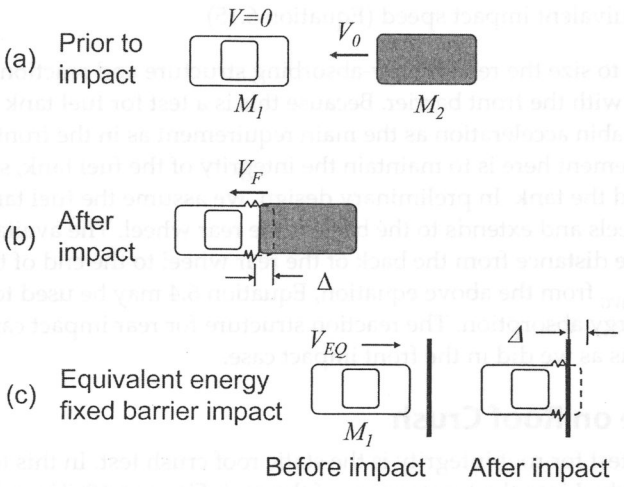

Figure 6.59 Rear impact equivalent fixed barrier test.

Now we can find the work of deformation, W, during the moving barrier impact, Figure 6.59b, by equating work to change of kinetic energy before and after the impact.

$$W = \frac{1}{2} M_2 V_0^2 - \frac{1}{2}(M_1 + M_2) V_F^2$$

$$W = \frac{1}{2}\left(\frac{M_1 M_2}{M_1 + M_2}\right) V_0^2$$

Finally we consider an impact with a fixed barrier which will cause the same work of deformation, Figure 6.59c and determine the equivalent impact velocity, V_{EQ}.

$$\frac{1}{2} M_1 V_{EQ}^2 = W$$

$$\frac{1}{2} M_1 V_{EQ}^2 = \frac{1}{2}\left(\frac{M_1 M_2}{M_1 + M_2}\right) V_0^2$$

$$V_{EQ} = V_0 \sqrt{\frac{M_2}{M_1 + M_2}} \tag{6.15}$$

Now using this fixed barrier equivalent velocity, we can identify the needed average rear crush force using

$$\frac{1}{2} M_1 V_{EQ}^{\ 2} = F_{AVG} \Delta$$
$$F_{AVG} = \frac{M_1 V_{EQ}^{\ 2}}{2\Delta} \tag{6.16}$$

where:

Δ = Available crush space between fuel tank and bumper

M_1 = Vehicle mass

V_{EQ} = Equivalent impact speed (Equation 6.15)

The process to size the rear-energy-absorbing structure and reaction structure is the same as with the front barrier. Because this is a test for fuel tank integrity, we do not use cabin acceleration as the main requirement as in the front barrier. The main requirement here is to maintain the integrity of the fuel tank, so all crush must occur behind the tank. In preliminary design, we assume the fuel tank is between the rear wheels and extends to the back of the rear wheel. The available crush space, Δ, is then the distance from the back of the rear wheel to the end of the car. After obtaining F_{AVG} from the above equation, Equation 6.4 may be used to size the rear rails for energy absorption. The reaction structure for rear impact can be sized using limit analysis as we did in the front impact case.

6.5 Note on Roof Crush

A standard test for roof integrity is the static roof crush test. In this test, a rigid platen is pushed into the front corner of the roof, Figure 6.60. The criterion for this test for FMVSS 216 is to develop a minimum level of crush force, *1½* times the vehicle weight, without deforming beyond a set distance, *5 in. (125 mm)*.

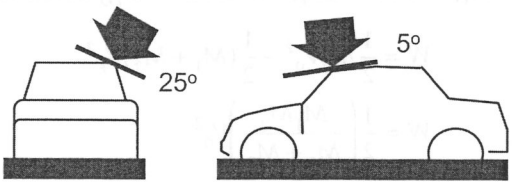

FMVSS 216
Load 1½ times vehicle weight
Criterion: Less than 5 inches of deformation

Figure 6.60 Static roof crush.

For preliminary structure sizing for this condition, we may again use limit analysis. A first-order model of side-view behavior is shown in Figure 6.61. Here the A pillar beam and roof side rail beam are connected by three plastic hinges: one at the belt line, one at the top of windshield, and one at the roof rail-to-B-pillar intersection. We ensure that the limit load exceeds the crush force requirement by applying the analysis procedures discussed earlier and shown in Figure 6.38. Note that this first-order model of roof crush neglects the often significant role the windshield plays in reacting the lateral component of the roof crush load.

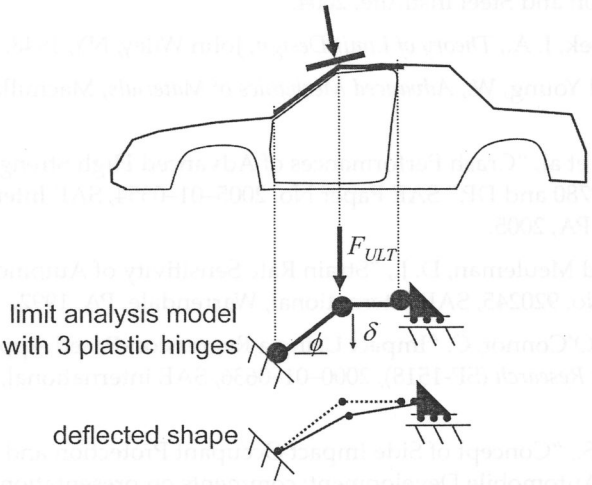

Figure 6.61 Limit analysis of roof crush.

References

1. *United States Federal Motor Vehicle Safety Standards and Regulations*, www.nhtsa.dot.gov/cars/rules/standards/safstan2.htm.
2. *Ultra Light Steel Auto Body-Final Report*, American Iron and Steel Institute, August 16, 1995.
3. Kikuchi, N. & Malen, D., Course notes for ME513 Fundamentals of Body Engineering, University of Michigan, Ann Arbor, MI, 2007.
4. Mahmood, H. F. and Paluszny, A., "Design of Thin Walled Columns for Crash Energy Management," SAE Paper No. 811302, SAE International, Warrendale, PA, 1981.
5. *Cold-Formed Steel Design Manual*, American Iron and Steel Institute, Washington, DC, 1986, Section 3.6.4.
6. Sidhu, R., et al, J., "Improved Vehicle Crashworthiness Via Shape Optimization," IMECE2003–43439, Society of Automotive Engineers, PA, 2003.
7. Sheh, M.Y. and Khalil, T.B. "The Impact Response of a Vehicle Structural Rail by Experiments and Finite Element Analysis," *Symposium on Crashworthiness and*

Occupant Protection in Transportation Systems, ASME Publication, AMD-Vol. 126/BED-Vol. 19, 1991, pp. 195–207.

8. Chang, D., "A Design-Analysis Method for the Frontal-Crush Strength of Body Structures," SAE Paper No. 770593, SAE International, Warrendale, PA, 1977.
9. Hamza, K. and Saitou, K., "Design Optimization of Vehicle Structures for Crashworthiness Using Equivalent Mechanism Approximations," *Journal of Mechanical Design*, AMSE, May 2005, pp. 485–491.
10. Prasad, P. and Belwafa, J. Editors, *Vehicle Crashworthiness and Occupant Protection*, American Iron and Steel Institute, 2004.
11. Van Den Broek, J. A., *Theory of Limit Design*, John Wiley, NY, 1948.
12. Cook, R. and Young, W., *Advanced Mechanics of Materials*, Macmillan Co., NY, 1985, p. 447.
13. Chen, X. M., et al, "Crash Performances of Advanced High Strength Steels of DP780, TRIP780 and DP," SAE Paper No. 2005–01–0354, SAE International, Warrendale, PA, 2005.
14. Shi, M. F. and Meuleman, D. J., "Strain Rate Sensitivity of Automotive Steels," SAE Paper No. 920245, SAE International, Warrendale, PA, 1992.
15. Deb, A. and O'Connor, C. "Impact Using a Regression-Based Approach," *SAE Side Collision Research* (SP-1518), 2000–01–0636, SAE International, Warrendale, PA, 2000.
16. Yamaguchi, S., "Concept of Side Impact Occupant Protection and Evaluation Method for Automobile Development; comments on presentation by J. Kanianthra," *SAE Stapp Car Crash Conference Proceedings*, SAE International, Warrendale, PA, 1993–1994.